*Clays and Clay Minerals*, Vol. 66, No. 1, 43–60, 2018.

# MINERALOGICAL EVOLUTION OF THE PALEOGENE FORMATIONS IN THE KYZYLTOKOY BASIN, KYRGYZSTAN: IMPLICATIONS FOR THE FORMATION OF GLAUCONITE

Tursunai Bektemirova[1,2,3,4,*], Apas Bakirov[4], Ruizhong Hu[1,3], Hongping He[2,3], Yuanfeng Cai[5], Wei Tan[2,3], and Aiqing Chen[2,3]

[1]State Key Laboratory of Ore Deposit Geochemistry, Institute of Geochemistry of Chinese Academy of Sciences, Guiyang 550002, Guizhou, China
[2]CAS Key Laboratory of Mineralogy and Metallogeny, Guangzhou Institute of Geochemistry, Chinese Academy of Sciences, Guangzhou 510640, China
[3]University of Chinese Academy of Sciences, Beijing 100049, China
[4]Institute of Geology, Kyrgyz National Academy of Science, 30 Erkindik Avenue, Bishkek 720481, Kyrgyzstan
[5]State Key Laboratory of Mineral Deposits Research, School of Earth Science and Engineering, Nanjing University, Nanjing, 210093 China

**Abstract**—Although several hypotheses for the formation of glauconite have been proposed, the sedimentary environment and mechanism of glauconitization are still poorly understood. In this contribution, the mineralogy and chemical compositions of sediments from Paleogene formations (Fms) in the Kyzyltokoy basin (Kyrgyzstan) were examined to better understand glauconitization processes. The samples were analyzed using microscopic petrography, X-ray diffraction (XRD), electron probe microanalysis (EPMA), and X-ray fluorescence (XRF). Interlayered diatomite-argillaceous rocks were newly identified within the diatomites of the Isfara Fm. Glauconite from the Kyzyltokoy basin displayed two stages of maturity: 1) early stage (nascent) glauconite grains composed of ~3.5% $K_2O$ and ~8% $FeO_T$; 2) late-stage (highly evolved) glauconite grains composed of 7−9% $K_2O$ and ~27% $FeO_T$. The early stage glauconite grains in the Hanabad Fm green clay (green clay is clay with a greenish color) indicate interruptions in glauconitization processes, whereas the (highly) evolved glauconite grains show a completed glauconitization process along the contact between the Hanabad and Sumsar Fms. Hematite was detected in the red clay (clay with reddish color) of the Sumsar Fm and probably formed by glauconite disintegration. Accordingly, the Paleogene Fms depositional conditions were of three types: 1) beginning of glauconitization with interruptions, 2) completion of glauconitization, and 3) glauconite disintegration. Glauconitization in the Kyzyltokoy basin, thus, likely occurred *via* a combination of dissolution, precipitation, and recrystallization processes.

**Key Words**—Crystallo-chemical Formula, Glauconite, Maturity, Mineralogy, Paleogene Formations, Sedimentary Environment.

## INTRODUCTION

Glauconite forms in slightly reduced and sub-oxic marine environments in association with other diagenetic minerals in organic-rich sediments (Burst, 1958; Odin and Matter, 1981; Odin, 1988; Amorosi, 1997). At low temperature, the substrate (*e.g.*, fecal pellets and microorganisms) provides a micro-reducing environment for the formation of glauconites (Harder, 1980; Huggett *et al*., 2017). Migration of K and Fe ions from seawater or the surrounding marine sediments controls the glauconitization processes (Harder, 1980; Meunier and El Albani, 2007). Glauconitization is a time-dependent process, thus, it can only be fully completed in low sedimentation-rate environments (Harder, 1980; Odin, 1988; Gaudin *et al*., 2005). The mechanism of glauconitization, however, has yet to be fully understood. Two hypotheses for glauconite formation have been proposed: 1) The "layer lattice theory" where degraded 2:1 expandable layers are transformed into 2:1 non-expandable layers with $Fe^{3+}$ substituting for $Al^{3+}$ in the octahedral sheet with a concomitant gradual increase in lattice charge (octahedral layer) and a consequent increase in interlayer K (Burst, 1958; Hower, 1961; Odom, 1984); 2) The "verdissement theory" where the substrate (phyllosilicate, K-feldspar, organic matter, and fecal pellets) is dissolved, an initial mineral (smectite) is precipitated, and it is recrystallized as glauconite (Keller, 1958; Odin and Matter, 1981; Odin and Fullagar, 1988; Kelly and Webb, 1999; Chang *et al*., 2008; Harding *et al*., 2014).

Glauconite maturation can be divided into four stages that depend on K content, pellet morphology, and crystalline structure, *i.e.*, 1) nascent; 2) slightly evolved;

* E-mail address of corresponding author:
tursunai@mail.gyig.ac.cn
DOI: 10.1346/CCMN.2018.064086

This paper was originally presented during the 3rd Asian Clay Conference, November 2016, in Guangzhou, China

3) evolved; and 4) highly evolved (Burst, 1958; Hower, 1961; Odom, 1984; Odin and Fullagar, 1988; Gaudin *et al*., 2005; Longuepee and Cousineau, 2006; Amorosi *et al*., 2011). In the nascent stage, the glauconite grains (2−4% $K_2O$) are pale-green in color, smaller in size, and enriched in biogenic particles. The grains in the slightly evolved stage have higher $K_2O$ contents (4−6%). The evolved (6−8% $K_2O$) and highly evolved (>8% $K_2O$) glauconite grains are dark green and larger (Odin and Matter, 1981; Amorosi, 1997; Huggett *et al*., 2017). Glauconite grains in the two late stages have a shinier or a polished appearance and a more fractured morphology. The ratio of glauconite to smectite layers also increases from nascent to the highly evolved stage and can serve as an important indicator of glauconite maturity (Burst, 1958; Hower, 1961; Odom, 1984; Odin and Fullagar, 1988; Kelly and Webb, 1999).

Clay minerals from the Kyzyltokoy basin (Kyrgyztsan) are poorly documented and a glauconite was newly identified in the present study. The Kyzyltokoy deposit is unique because a complete glauconitization history as well as the processes before and after (*i.e*. disintegration) glauconitization have been recorded in the Paleogene formations (Fms) (from the Rishtan to the Sumsar Fms). The present study aimed to investigate the chemical composition and genesis of glauconites from the Kyzyltokoy basin by using a combination of X-ray diffraction (XRD), X-ray fluorescence (XRF), and electron probe microanalysis (EPMA). The results of the present study will be important in understanding the evolution of paleoenvironments in this area and for the utilization of clay mineral resources.

## GEOLOGICAL SETTING

The Kyzyltokoy deposit is located in the northeastern part of the Fergana depression and on the southern slope of the Chatkal ridge, which is part of the Chatkal-Kuramin fold belt of the Kyrgyz Middle Tian Shan. This area is characterized by gypsum-bearing Paleozoic sediments and by Cenozoic marine deposits (Figure 1).

### *Paleogene stratigraphy*

The stratigraphy of the Paleogene sediments in the Kyzyltokoy basin includes eight fossil-defined Paleogene Fms, *i.e*., the Bukhara, Suzak, Alai, Turkestan, Rishtan,

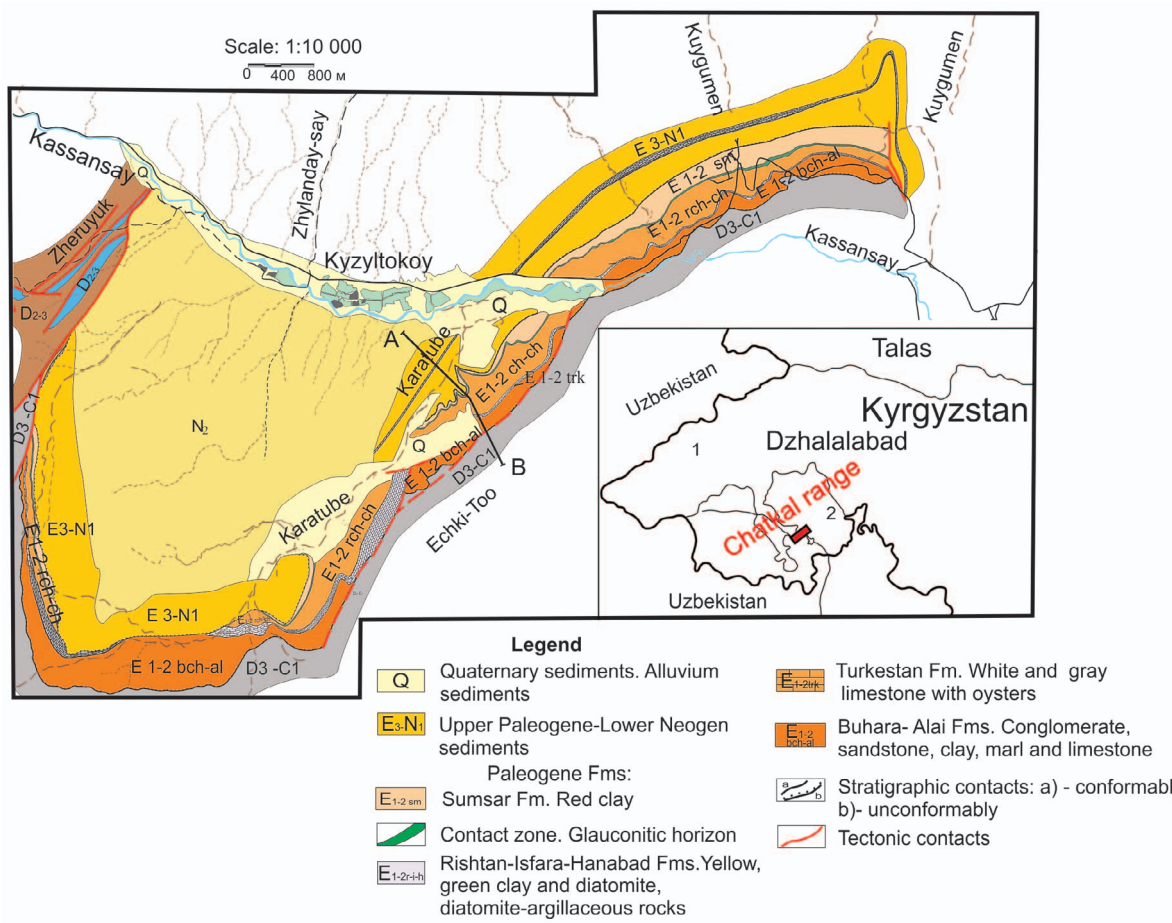


Figure 1. Geological map of the Kyzyltokoy Basin (after Bakirov *et al*., 2011). Fms = Formations; Fm = formation.

Isfara, Hanabad, and Sumsar Fms (Bakirov *et al*., 2011). The upper Oligocene sediments are locally represented by the Massaget series, which conformably overlie the Sumsar Fm (Vyalov, 1947). The total thickness of the Paleogene (Paleocene-Eocene) sediments of the Kyzyltokoy basin vary from 110 to 200 m.

According to the field study, the Paleogene Fms show an erosional disconformity with the underlying Paleozoic sedimentary rocks and are unconformably overlain by the Upper Paleogene - Lower Neogene Massagetan Fm (Figure 2b). The Paleogene marine sediments extend as a narrow strip along the periphery of the Kyzyltokoy syncline (Figure 1). The main study area included the Upper Eocene Rishtan, Isfara, Hanabad, and Sumsar Fms. Glauconite outcrops were found in the Hanabad Fm and along the contact between the Hanabad and Sumsar Fms (Figures 1 and 2).

*The Rishtan Fm* lower part is 8 m thick and is represented by a yellow clay that contains oyster shells. The overlying unit (about 6 m thick) is composed of a grayish-yellow siliceous clay and, in general, the formation is 15 m thick.

*The Isfara Fm* is represented by diatomite, interlayered with ~4-m thick, yellowish-brown, sandy diatomite-argillaceous rocks and the general thickness of the Isfara Fm is 16–20 m.

*The Hanabad Fm* features a 10-m thick green clay (Figures 3b, 3h). The sediment is called a green clay due to the clayey texture and the green color. In the sediments, foraminifer remnants and traces of white tubular fossils are abundant. In the upper part of the formation along the 1–5 m thick contact zone with the red clay of the Sumsar

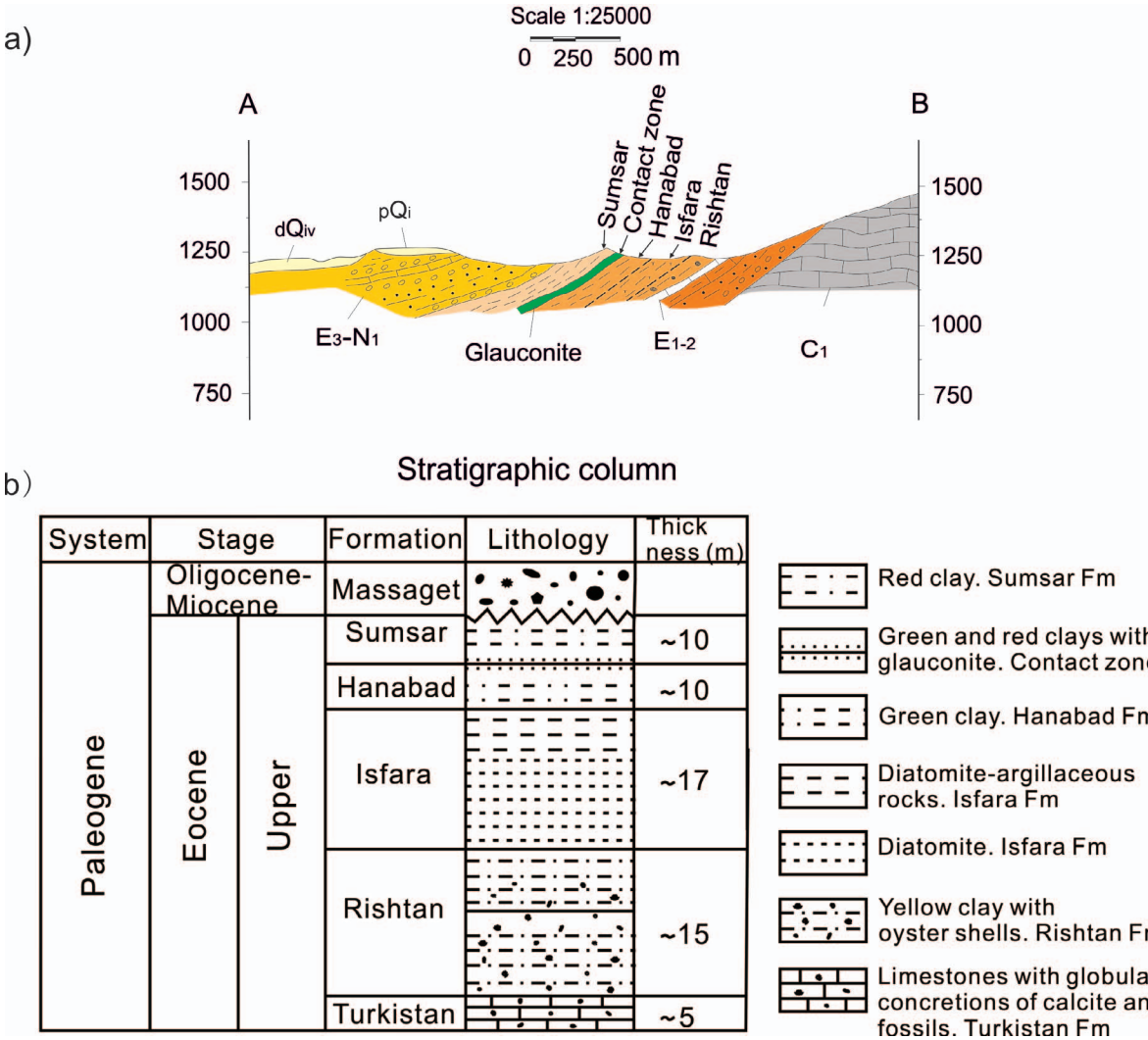


Figure 2. a) Cross section and b) Stratigraphic column of the Paleogene Formations in the Kyzyltokoy Basin (after Bakirov *et al*., 2011).

Table 1. Size distribution of glauconite from the contact zone.

| Samples | Grading (size distribution in %) | | | | | | |
|---|---|---|---|---|---|---|---|
| | <0.15 mm | >0.15 mm | >0.2 mm | >0.3 mm | >0.45 mm | >0.9 mm | Σ |
| Contact zone Sample 1511 | 36.3 | 11.0 | 27 | 16 | 9.0 | 0.04 | 99.34 |
| Contact zone Sample 14 | 5.8 | 2.7 | 31 | 38 | 20.0 | 2.06 | 99.56 |
| Contact zone Sample 31 | 6.5 | 7.8 | 29 | 35 | 21.2 | 0.80 | 100.30 |

Fm, the rock is replaced by a greenish/red clay with abundant glauconite (Figures 2a, 2b).

*The Sumsar Fm* is represented by a red clay (Figures 3g, 3h). The upper part of the formation contains a 3−5 m thick clay layer with thick-walled oyster shells, foraminifers, ammonites, brachiopods, gastropod remnants, and shark teeth with a total formation thickness of about 10−15 m.

*The Massaget Fm* (Upper Paleogene−Lower Neogent) is composed of reddish continental, sandy-conglomeratic sediments that unconformably overlie the Sumsar Fm (Upper Eocene).

## SAMPLES AND METHODS

The samples from the Paleogene sediments were collected from eight sections. In the laboratory, all samples were crushed and sieved to obtain the clay fractions (Table 1). Glauconite concentrates were obtained from the clays by washing, magnetic separation, and handpicking under a binocular microscope. The powder samples were placed in bottles with 200 mL of distilled water, and sodium hexametaphosphate (SHMP) was added as a dispersing agent to break down clay aggregates for textural analysis. The mixtures were shaken for 30 min using ultrasonic disaggregation to reduce the particle size without structurally changing the clay minerals. Afterwards, the samples were treated with disodium ethylenediamine tetraacetic acid dehydrate (EDTA) for 8 h at room temperature and washed with distilled water to remove gypsum, which inhibits enzyme-catalyzed reactions. To eliminate calcite and any carbonate cement, the samples were acid-treated with 1.2 M HCl for about 3 to 4 h. The clay mineral particles (<10 μm) were then separated using centrifugation.

Powder X-ray diffraction (XRD) patterns of nine samples (1536, 1538, 1539, 1540, 1542, 1511, 1545, KT-02, and 1547) were obtained using a Bruker D8 Advance diffractometer (Bruker, Karlsruhe, Germany) with Ni filtered CuKα radiation (λ = 0.154 nm, 40 kV, and 40 mA), a scanning rate of 1º2θ $min^{-1}$, and were scanned from 2º to 65º2θ in the Guangzhou Institute of Geochemistry, Chinese Academy of Sciences, China. The XRD patterns of other samples were obtained using a DRON-4 diffractometer with CuKα radiation (pr. Burevestnik, Sankt Peterburg, Russia) in Almaty, Kazakhstan.

Clay mineralogy (bulk composition) of the sediments was determined using the Bruker diffractometer and oriented, glycol solvated (8 h at 60ºC), and heated (2 h at 450ºC) samples using the methods of Moore and Reynolds (1997). Semi-quantitative mineral compositions were calculated from the XRD patterns using MDI Jade software (MDI, Livermore, California, USA). The relative abundances of clay-mineral species were mainly estimated by using the areas of the (001) series of basal reflections, *i.e.* smectites (15 Å), I-S (11−13 Å), illite/glauconite (10 Å), and kaolinite/chlorite (7 Å). Because it is difficult to distinguish glauconite from illite using powder XRD patterns due to the similar mica-like structures, the estimated glauconite and illite percentages are given in Figure 5.

The chemical composition of glauconite and glauconitic rocks was determined using XRF and EPMA. Clay samples that included glauconite were analyzed using a Bruker S8 Tiger XRF instrument (Bruker, Karlsruhe, Germany) at the Department of Geology, University of Tromsø. To determine the elemental composition, fused glass discs were prepared from 1.0-g milled samples mixed with 9.0 g of flux (34% $LiBO_2$ and 66% $Li_2B_4O_7$).

A four wavelength-dispersive JEOL JXA-8800M electron-microprobe analyzer (JEOL, Tokyo, Japan)

Figure 3 (*facing page*). a) Concentrated glauconite grains. b) Fine-grained, light green glauconite particles from the green clay of the Hanabad Fm. c) A sample from the western part of the contact zone that contains glauconite grains from within the semi-oxidized zone. d, e, f) Larger, dark green glauconite particles from the central and eastern parts of the contact zone; The grains in (d) and (f) had light green edges and spots. g) Partially dissolved glauconitic grains from the Sumsar Fm red clay. h) The contact zone between the green clay of the Hanabad Fm and red clay of the Sumsar Fm. Gl = glauconite; Cc = calcite; Fe-ox/hydro = Fe-oxide/oxyhydroxide; OM = Organic Matter; Gr. cl = green clay; Red. cl = red clay.

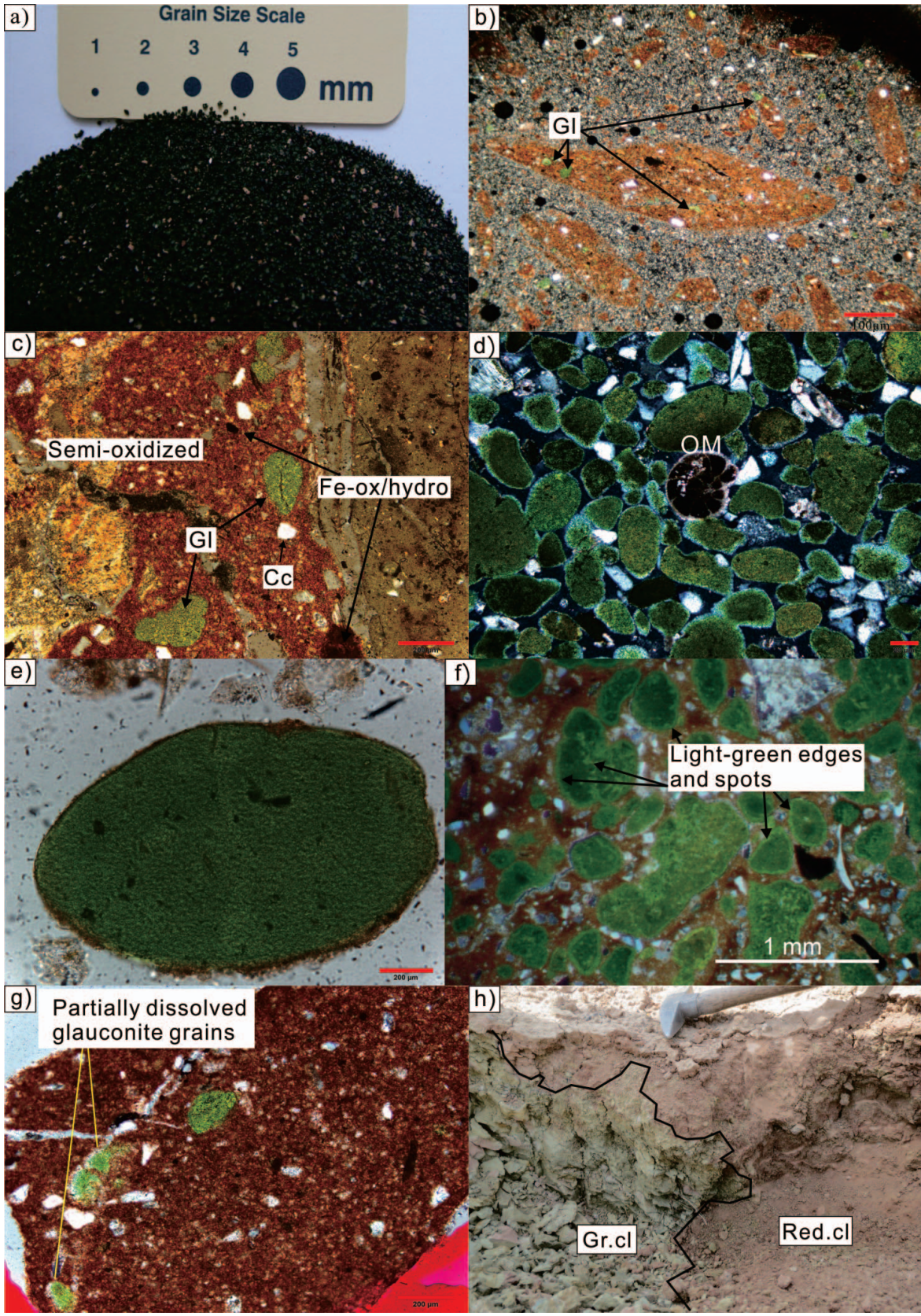

was used to study the glauconite samples at the Department of Geoscience, University of Shimane (Japan). Operating conditions included a 15-kV accelerating voltage, a 20-mA beam current, a beam diameter of 5 μm, a background count time of 5 s, and a measurement time of 10 s.

## RESULTS

### *Mineral components*

The glauconite grains studied were commonly irregular, ellipsoidal, and globular particles (Figure 3). The grains in the green clay of the Hanabad Fm were light green and much finer in size (a few μm) (Figure 3b). Grains from the contact zone (between the Hanabad and Sumsar Fms) were green to dark green and were mostly fractured (Figures 3c, 3d, 3e, and 3f). The grain size in this zone varied in the western (~0.3 mm), central (~0.7 mm), and eastern parts (~0.4 mm) of the Kyzyltokoy basin (Figures 3c, 3d, 3f, and 3g). A semi-oxidized zone and glauconite grains were observed in the samples of the contact zone (Figure 3c) from the western part, but no glauconite was observed outside this zone. Organic matter (*e.g.*, foraminifer and gastropods), Fe-Ti oxide particles, and other detrital minerals (*e.g.*, quartz, calcite, albite, and orthoclase) were detected by microscopic observation (Figures 3c, 3d, 3f). In the red clay of the Sumsar Fm (early stage), partially dissolved glauconitic grains were observed (Figure 3g). As quantified from the XRD patterns, the green clay of the Hanabad Fm contained about 10−15% glauconite in the rocks (Figure 3b). The contact zone samples contained about 30% glauconite and the western and central/eastern parts of the Kyzyltokoy basin samples contained 40−50% glauconite (Figures 3c, 3d, 3f). The XRD patterns of the sediments (Figures 4 and 5) revealed that smectite, glauconite, illite, and mixed-layered minerals were the dominant clay minerals. The air-dried sample glauconite peaks included a (001) basal reflection at 10.5 Å, a (020) reflection at 5.0 Å, a (003) reflection at 3.32 Å, and a 4.57 Å peak (Figures 6d, 6e). After glycolation, the (001) reflection slightly shifted from 10.4 to 9.5 Å, while (020) and (003) reflections were unchanged.

*Rishtan Fm (yellow clay)*: The intense and broad XRD reflection at approximately 14.5 Å in the air-dried sample moved to 17 Å with a 15 Å shoulder after glycolation (Figure 6a). After heat treatment, the 14.5 Å reflection became very weak, while the 10 Å reflection became more intense, which suggests the presence of smectite in the sample. The chlorite content was negligible because the characteristic reflections at 14 Å, 7.14 Å, and 3.55 Å could not be distinguished. Illite (15.5%), quartz (~40%), gypsum (~14%), calcite (~11%), and albite (~4%) were detected, but no glauconite (Figures 4 and 5). No glauconite was identified in the air-dried, glycolated, and heated samples (Figure 6a). The smectite content (22%) was much higher than in the samples from the Isfara Fm (Figure 4, sample 1536).

*Isfara Fm (diatomite and diatomite-argillaceous rocks)*: Silica (quartz and opal) was abundant in these samples. Diatomite (samples 1538 and 1539) contained a higher quartz content (~70%) than the diatomite-argillaceous rocks (~51% quartz) (Figure 4, sample 1540). The smectite content was higher (14%) than illite (9%) in the diatomites, whereas the illite content (19%) in the diatomite-argillaceous rocks was higher than smectite (15%). About 4% albite and 5% microcline were detected in both samples (Figures 4 and 5). A 4.56 Å peak (air-dried) was not observed in these samples, however, and the mica-like structure mineral should be illite rather than glauconite (Figures 6b and 6c).

*Hanabad Fm (green clay)*: More mixed layer minerals and glauconite were detected in the green clay of the Hanabad Fm than in samples of the Rishtan and Isfara formations (Figure 5). A broad reflection at 10.57 Å (air-dried), which split into two reflections 9.98 Å (intense) and 10.92 Å (weaker) after glycol saturation, indicated the presence of an interstratified mineral (smectite-glauconite) (Velde and Odin, 1975) (Figure 6d). This suggests that it contained a higher percentage of expandable layers. The air-dried samples had a (001) basal reflection at 10.5 Å, a (020) reflection at 5.0 Å, a (003) reflection at 4.57 Å, and a 3.34 Å peak (Figure 6d). Hence, the mica-like mineral was glauconite rather than illite, which was also deduced from the green color, petrographic examination, and the chemical studies.

Based on the XRD patterns, the mineralogical components of the green clay included smectite (~19%), kaolinite (~5%), gypsum (~15%), calcite (~7%), quartz (~38%), microcline (~4%), and a small amount of pyrite. The smectite-glauconite mixed-layer mineral (MLM) content was much higher (~13%) and the glauconite content was much lower in these samples than in the samples from the contact zone.

*Contact zone (glauconite)*: The glauconite content was about 28% and was obviously higher than the underlying formation. The XRD reflection at approximately 15 Å in the air-dried sample patterns corresponds to a smectite (about 13%; Figure 6e). The samples also contained ~3% chlorite, ~6% calcite, and negligible pyrite. In the extracted glauconite samples, the glauconite content was ~82%, while the smectite content was about 5% (bulk composition). It also contained minor amounts of detrital minerals, such as calcite (~5%), quartz (~3%), and albite (~3%) (Figure 5). The contact zone and Hanabad Fm sample mineral components had an increased glauconite content as the smectite content decreased (Figures 5, 6d, and 6e).

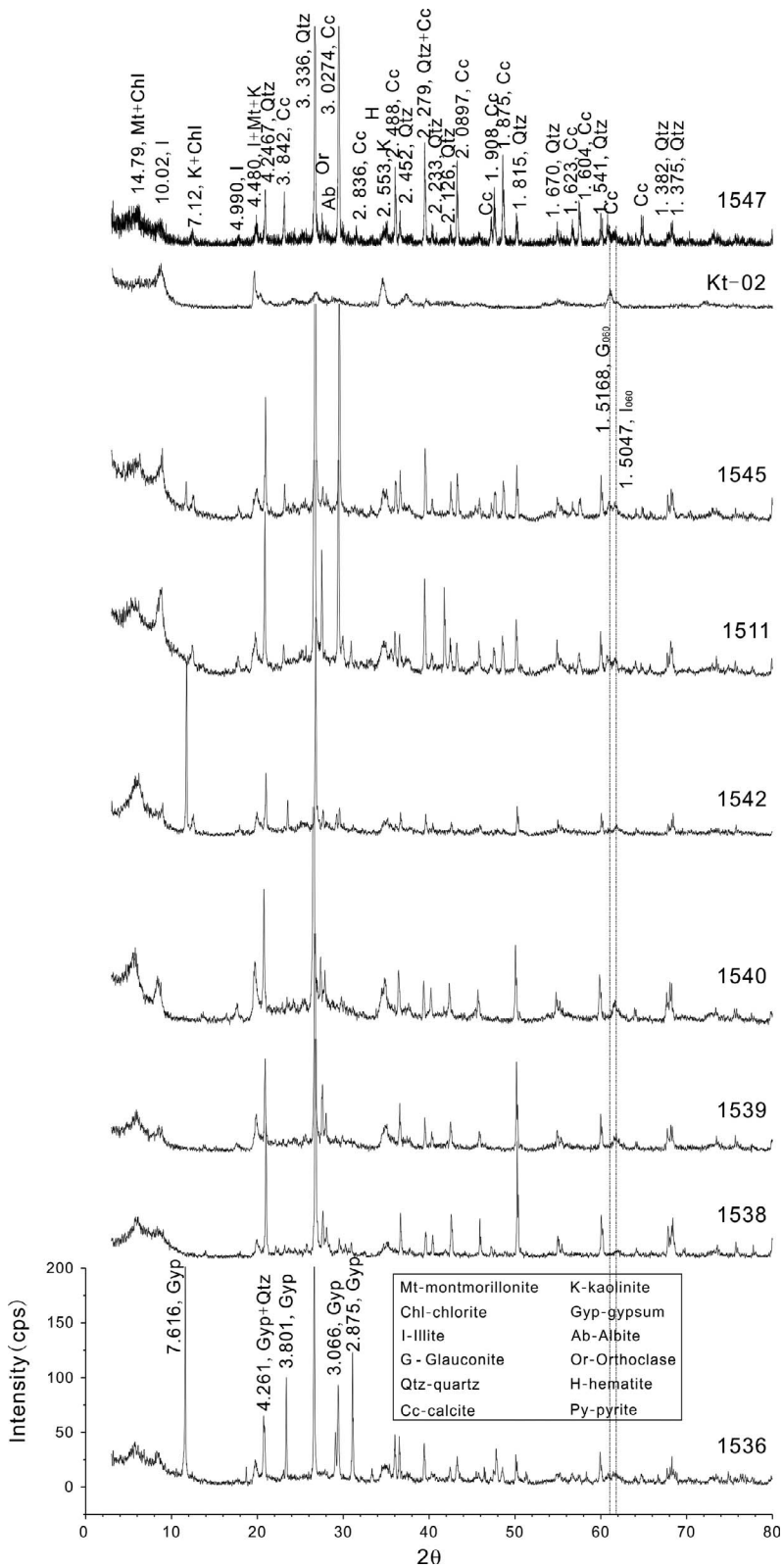


Figure 4. Powder XRD patterns of the Paleogene Fms samples: sample 1536 = yellow clay; samples 1538 and 1539 = diatomite; sample 1540 = diatomite-argillaceous rock; sample 1542 = green clay; samples KT-02, 1511, and 1545 were from the contact zone; and sample 1547 = red clay.

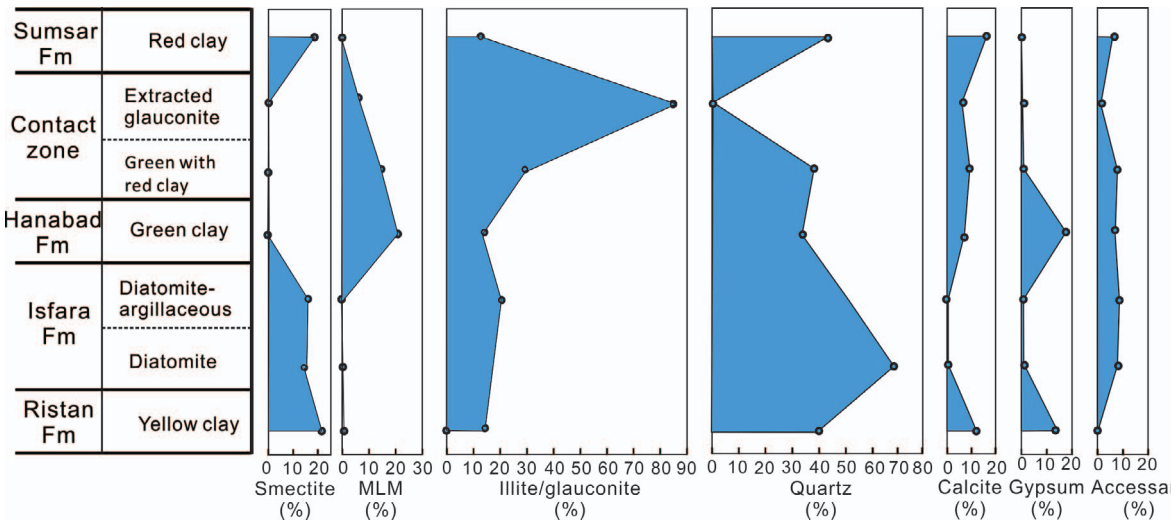


Figure 5. Mineral compositions of samples from the Paleogene Fms. MLM = mixed-layered mineral.

*Sumsar Fm (red clay)*: Minor hematite (shown by very weak XRD reflections) was detected in the red clay (Figures 4 and 5) and probably formed from the disintegration of glauconite. The XRD patterns indicated the following mineral components: smectite (~18%), illite (~13%), quartz (~49%), chlorite (~2%), and calcite (~16%) (Figure 5).

*Bulk-sediment XRF chemistry of the Paleogene formations*

The major element oxide distributions in the samples from the Paleogene Fms differed from one formation to another (Table 2).

*Rishtan Fm (yellow clay)*: The yellow clay samples contained ~42% $SiO_2$, 8.4% $Al_2O_3$, 3.4% $Fe_2O_{3T,}$ and 2.1% MgO. The

Table 2. Major element composition of the yellow clay, diatomite, diatomite-argillaceous rocks, green clay, and red clay as well as the contact zone greenish-red clay.

| Sample (%) | $SiO_2$ | $Al_2O_3$ | $Fe_2O_3$ | MgO | $TiO_2$ | MnO | CaO | $K_2O$ | $Na_2O$ | $P_2O_5$ | $CO_2$ |
|---|---|---|---|---|---|---|---|---|---|---|---|
| Yellow clay | | | | | | | | | | | |
| 199 | 44.44 | 10.20 | 4.34 | 2.68 | 0.59 | 0.11 | 11.45 | 2.35 | 0.14 | 0.10 | 23.59 |
| 243 | 32.67 | 4.99 | 1.91 | 0.93 | 0.28 | 0.10 | 30.47 | 1.17 | 0.23 | 0.47 | 26.78 |
| 244 | 44.54 | 9.02 | 3.66 | 2.37 | 0.46 | 0.41 | 16.49 | 2.21 | 0.28 | 0.21 | 20.35 |
| Diatomite and diatomite-argillaceous rocks | | | | | | | | | | | |
| Dt 247 | 72.77 | 9.81 | 4.12 | 1.12 | 0.53 | 0.02 | 0.93 | 3.30 | 0.89 | 0.15 | 6.08 |
| Dt 253 | 65.99 | 11.99 | 4.73 | 1.89 | 0.63 | 0.01 | 1.80 | 3.43 | 0.52 | 0.21 | 9.72 |
| Dt-arg 46 | 65.93 | 15.29 | 2.39 | 2.43 | 0.79 | 0.02 | 0.41 | 3.37 | 0.34 | 0.05 | 8.84 |
| Dt-arg 256 | 53.71 | 12.46 | 4.89 | 2.24 | 0.54 | 0.04 | 6.50 | 3.50 | 0.47 | 0.19 | 16.48 |
| Green clay | | | | | | | | | | | |
| 143 | 54.17 | 14.90 | 6.70 | 3.53 | 0.76 | 0.04 | 1.58 | 3.50 | 0.81 | 0.14 | 13.17 |
| 162 | 56.66 | 14.64 | 7.03 | 3.41 | 0.78 | 0.04 | 0.96 | 3.60 | 0.94 | 0.14 | 10.16 |
| 222 | 44.26 | 8.96 | 6.22 | 2.12 | 0.48 | 0.16 | 15.72 | 3.50 | 0.28 | 0.46 | 18.86 |
| 223 | 41.16 | 9.10 | 6.91 | 2.66 | 0.41 | 0.15 | 15.34 | 3.91 | 0.26 | 0.92 | 18.88 |
| Contact zone | | | | | | | | | | | |
| 227 | 49.85 | 7.51 | 8.50 | 3.14 | 0.67 | 0.05 | 5.52 | 4.93 | 0.69 | 0.16 | 16.03 |
| 228 | 46.20 | 9.48 | 7.74 | 2.62 | 0.50 | 0.11 | 10.90 | 5.19 | 0.50 | 0.61 | 16.95 |
| 229 | 46.73 | 8.40 | 7.70 | 2.90 | 0.51 | 0.11 | 12.37 | 5.50 | 0.44 | 0.30 | 16.29 |
| 82(gl.gr) | 45.71 | 3.41 | 29.02 | 3.47 | 0.03 | 0.06 | 0.59 | 7.80 | 0.03 | 0.14 | 9.76 |
| Red clay | | | | | | | | | | | |
| 165 | 47.98 | 14.32 | 5.81 | 3.04 | 0.70 | 0.08 | 10.95 | 3.41 | 0.17 | 0.09 | 13.44 |
| 165a | 48.64 | 14.27 | 5.78 | 3.26 | 0.64 | 0.08 | 10.54 | 3.50 | 0.20 | 0.13 | 12.95 |
| 240 | 49.63 | 12.52 | 4.98 | 3.26 | 0.63 | 0.09 | 9.66 | 3.16 | 0.52 | 0.15 | 15.40 |
| 230 | 49.70 | 12.79 | 5.79 | 3.19 | 0.62 | 0.10 | 11.03 | 3.16 | 0.55 | 0.15 | 12.92 |

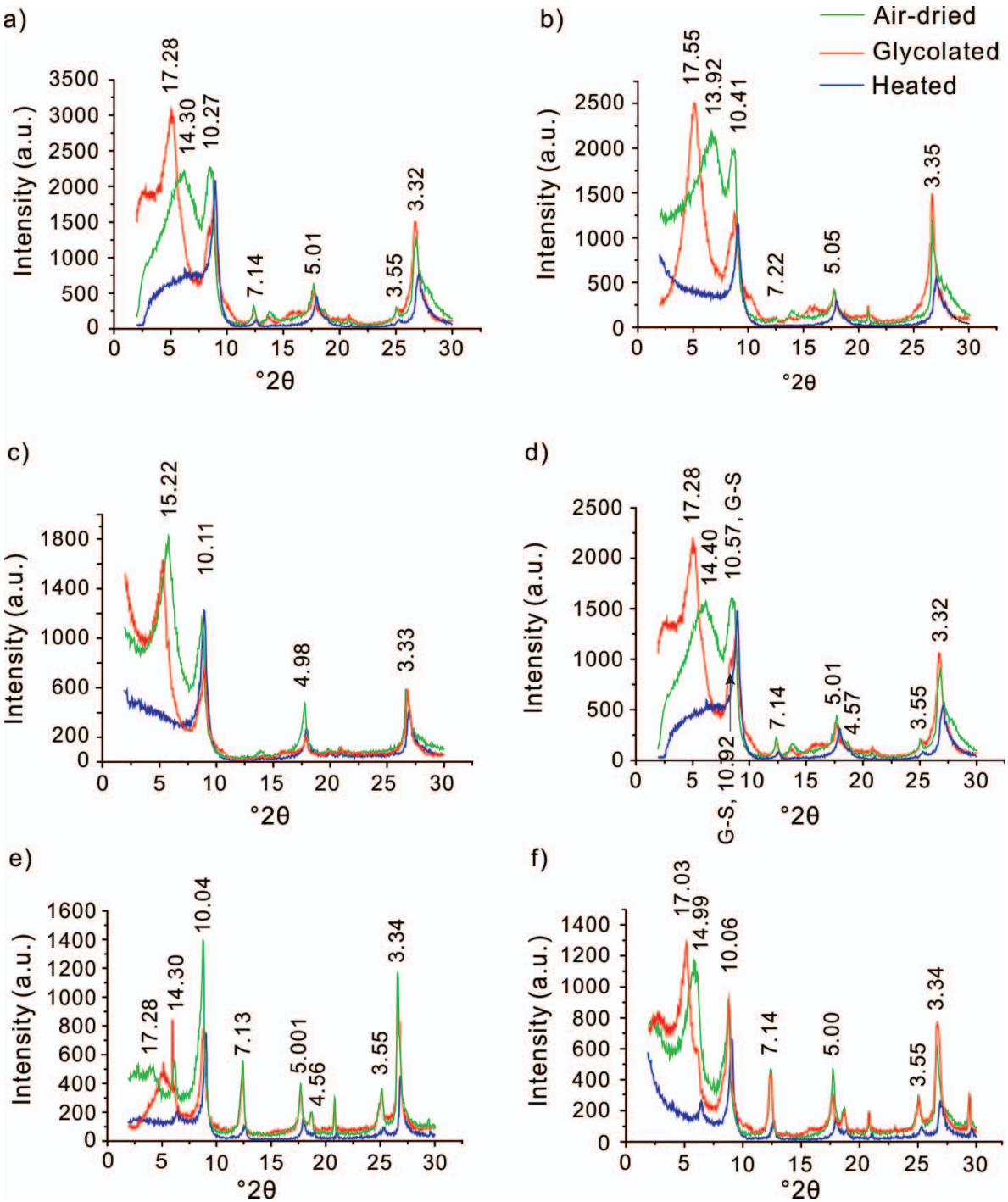


Figure 6. XRD patterns of the air-dried, glycolated, and heated samples from the Paleogene Fms: a) yellow clay from the Rishtan Fm; b) diatomite; c) diatomite-argillaceous rocks of the Isfara Fm; d) green clay of the Hanabad Fm; e) contact zone samples; and f) red clay of the Sumsar Fm. G-S = glauconite-smectite.

$K_2O$ content was ~2.2% and the $Na_2O$ content was ~0.23%. Small quantities of other element oxides, such as $TiO_2$ (0.53%), MnO (0.3%), and $P_2O_5$ (0.2%) were also measured in the samples. The CaO content was relatively high (~19%) in comparison to the upper formations.

*Isfara Fm (diatomite and diatomaceous-argillaceous rocks).* The major element oxide contents in the diatomite and the diatomite-argillaceous rocks varied. The $SiO_2$ content was higher in diatomite (~69%) than in the diatomite-argillaceous rocks (about ~59%). The

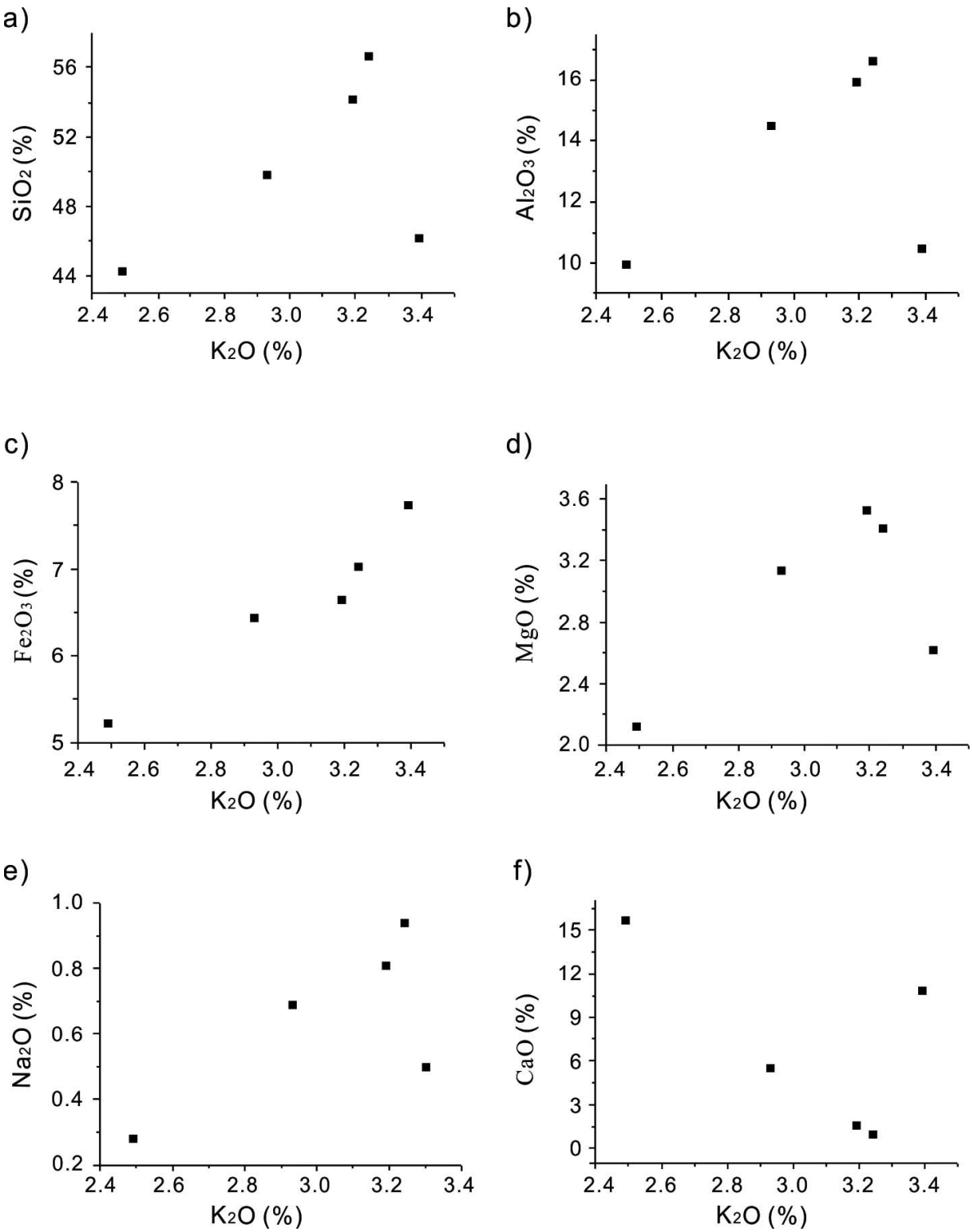


Figure 7. Correlation between the green clay $K_2O$ contents and the a) $SiO_2$, b) $Al_2O_3$, c) $Fe_2O_3$, d) MgO, e) $Na_2O$, and f) CaO contents.

$Al_2O_3$ content was ~10% in the diatomite and ~15% in the diatomite-argillaceous rocks. The MgO contents were 1.5% in the diatomite and 2.3% in the diatomite-argillaceous rocks. The diatomite-argillaceous rock CaO contents (4.15%) were greater than those in the diatomite (0.67%). The differences in the $Na_2O$ contents

were small (0.34% *vs*. 0.5%). The $Fe_2O_3$ contents increased with proximity to the diatomite-argillaceous rocks (~2.4% *vs*. ~4.8%) and had comparable values as the overlying formation. The $K_2O$ contents were ~3.3% in both samples, and increased slightly in the green clay of the Hanabad Fm.

*Hanabad Fm (green clay)*: The total $Fe_2O_3$ contents were ~7% and the $K_2O$ contents were ~3.65%. The $SiO_2$ contents were ~50.23% and the $Al_2O_3$ contents were ~13.5%. A slightly positive correlation was found between all the major element oxide ($SiO_2$, $Al_2O_3$, $Fe_2O_3$, MgO, and $Na_2O$) contents and the $K_2O$ content, but a negative correlation between the CaO content and the major elements (Figures 7a–7f). The $Al_2O_3$ and $Fe_2O_3$ contents of the green clay were positively correlated (Figure 8a). Using the Velde and Odin (1975) assumption that illite can be distinguished from glauconite by the Fe content when the alkali content is high (a mica-like phase), a diagram to relate alkali content ($Na_2O+K_2O$) to total Fe was constructed. The higher Fe contents in the plot indicate the glauconite-smectite series of the MLM phase (Figure 8b).

*Contact zone (glauconite)*. The $K_2O$ contents of the contact zone samples were much higher (~8%) than the Hanabad Fm green clay samples. The total $Fe_2O_3$ content (29%) was relatively high and the CaO content was 0.6% lower than that of the lower and upper formations.

*Sumsar Fm (red clay).* The sample chemical compositions (especially $Fe_2O_3$, CaO, and $K_2O$) differed in the lower and upper parts of the formation. In the lower part (close to the contact zone), the $Fe_2O_3$ (~7%) contents were higher than in the upper part (~3.4%). The $K_2O$ contents (~3.2%) were higher in the lower part than in the upper part (1.2%). The CaO (~14.4%) contents were low in the lower part, but high in the upper part (~20.1%). The $SiO_2$ (~43%) contents were almost the same in all parts of the Sumsar Fm and the $Al_2O_3$ contents were about 9%. The contents of other element oxides, such as MgO (~2.4%), MnO (~0.12%), $Na_2O$ (~0.4%), and $TiO_2$ (~0.4%), were minor in all samples.

*EPMA chemistry of the extracted glauconite grains*

The difference in the colors of the edges and spots of the glauconite grains probably reflects compositional variations, especially for total Fe and $Al_2O_3$ (Odin, 1988; Velde and Odin, 1975). The $SiO_2$ contents increased discontinuously from the core (47.58%–48.39%) to the rim (52.06%–49.72%) of the grains. The $Al_2O_3$ contents increased from the core (2.48%–3.57%) to the rim (5.07%–6.39%), which means that the rim was richer in Al than the center part. In contrast, the total Fe contents decreased steadily towards the rims (from 29.17% to 23.39%). The MgO contents mostly decreased from the center to the outermost parts of the grains (3.71–3.57%). The $K_2O$ contents varied across grains as well as between different grains, but mostly increased from rim to core and ranged from 6.51% to 9.04% with an average value of 8.21% (Figure 9). The $K^+$, $Al^{3+}$, and total $Fe^{2+}$ contents for mineral formulas were calculated for glauconite grains from the contact zone and compared to the formulas of grains of the Hanabad Fm green clay (Figure 10, Table 3).

The high alkali ($Na_2O+K_2O$) (~7.91%) and Fe contents indicate a distinct mixed-layered mineral series (Velde and Odin, 1975; Longuepee and Cousineaou, 2006). The alkali values ($Na_2O+K_2O$) and Fe contents in the diagram correspond to a glauconite-smectite phase (Figure 11).

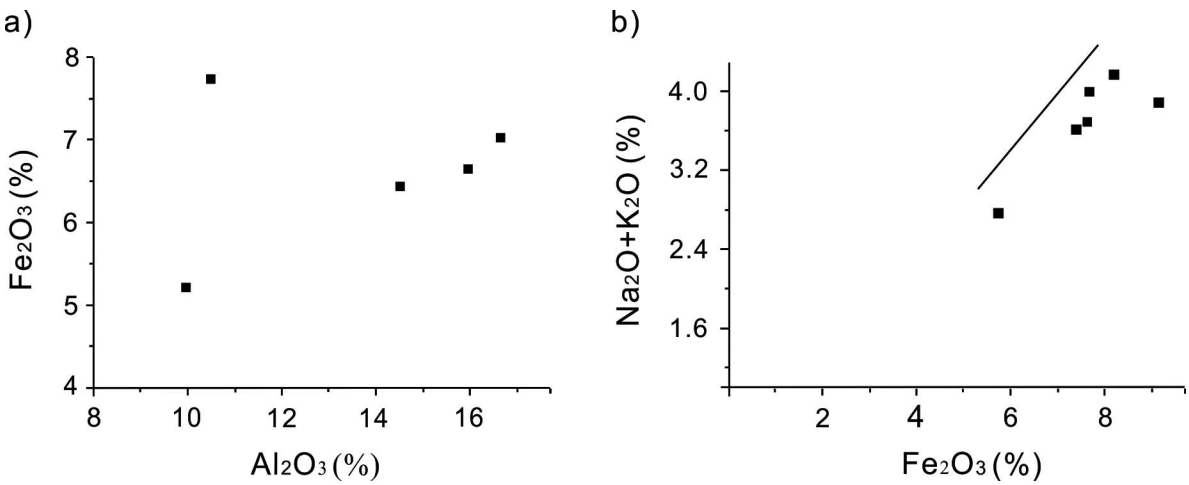


Figure 8. Relationship between a) the total $Fe_2O_3$ and $Al_2O_3$ content and b) the alkali ($Na_2O+K_2O$) and total $Fe_2O_3$ contents (wt.%) for the green-clay glauconite-smectite series (Velde and Odin, 1975).

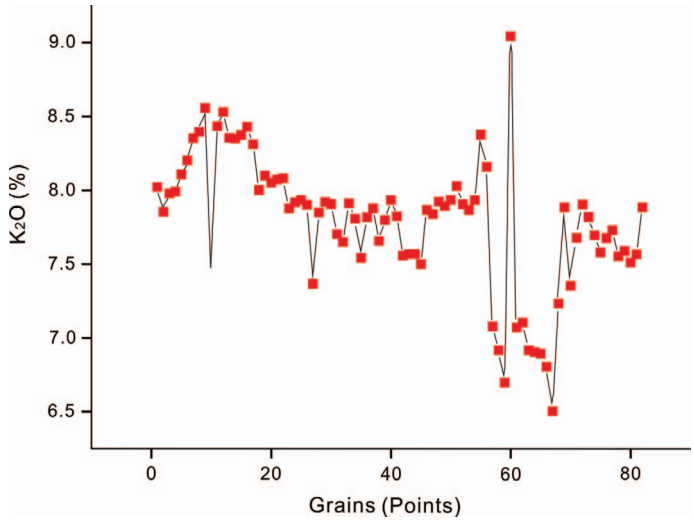


Figure 9. The variation in the $K_2O$ contents of sample glauconite grains indicates the different stages in glauconite evolution from evolved to highly evolved.

*Crystallo-chemical formulas of glauconite*

Cations in the mineral formula (Table 3) were calculated based on 10 oxygens and 2 hydroxyls, *i.e.* a half unit cell (Kelley, 1952; Afanasjeva *et al*., 2012) using EPMA data (Table 4). The Fe valences and glauconite crystallo-chemical formulas at the different stages were calculated using the methods of Kelley (1952) and Zheng (1983). In order to calculate mineral formulas from a chemical analysis (Table 4), the analytical data were first converted into molecular equivalents and then the cation equivalents were converted into charge equivalents. Alternatively, the oxygen equivalents can be calculated for each cation. The next step is to convert the cation charge equivalents calculated from the chemical analyses into cation charges for a specified number of total charges for the mineral unit cell, which contains 20 oxygens and 4 $OH^-$ or a total of 44 negative charges. The last step is to convert charges for each cation into the number of cations by dividing each by the valence. Alternatively, when formulas are calculated using oxygen equivalents, the oxygen equivalents are used to calculate cations per 22 oxygens (with an oxygen equivalent of 44 negative charges). Both methods produce similar results. Thus, the ions are distributed into the tetrahedral and octahedral positions. The Si goes to tetrahedral positions. The Si deficiency (8 - #Si) per formula unit is made up with Al in tetrahedral coordination. The remaining Al, Fe, and non-exchangeable Mg are placed in octahedral sites. All the exchangeable cations are placed in interlayer positions (Table 3). Zheng (1983) described in detail how to use several equations to

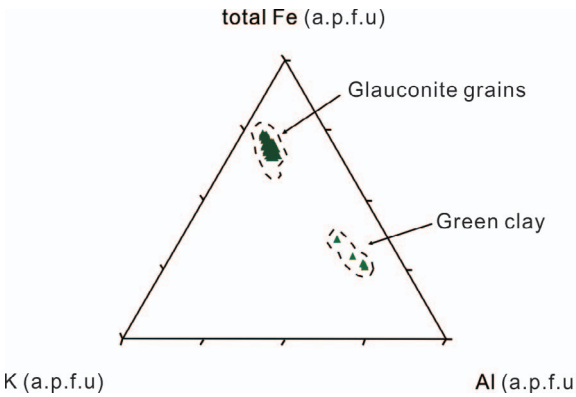


Figure 10. Three component diagram to compare the $K^+$, $Fe^{2+}$ (total), and $Al^{3+}$ contents (atoms per formula unit, a.p.f.u.) of glauconite grains from the Hanabad Fm green clay and the contact zone (Giresse and Wiewiora, 1999).

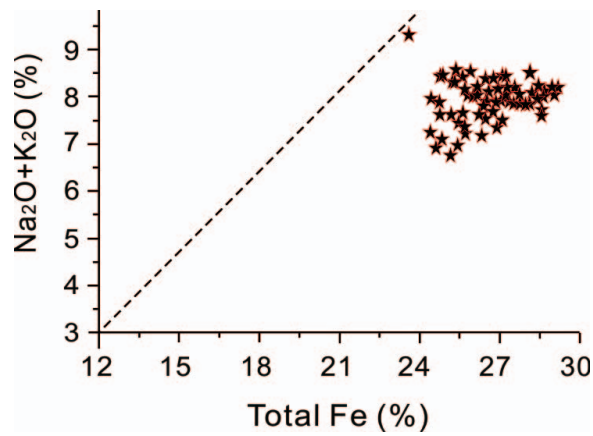


Figure 11. The relationship between alkali ($Na_2O+K_2O$ interlayer cations) and Fe (total FeO) contents in evolved glauconite samples (modified after Velde and Odin, 1975) and indicate the high Fe content specific to glauconite-smectite MLM (mixed-layer minerals).

Table 3. The crystallo-chemical formulas of glauconite in the nascent and evolved stages.

| Formations | Samples | Mineral Formulas |
|---|---|---|
| Hanabad | 143 | $(Na_{0.11}\ K_{0.3}\ Ca_{0.12})_{0.53}(Mg_{0.4}\ Fe^{2+}_{0.63}\ Fe^{3+}_{0.03}\ Al_{1.04})_{2.13}\ (OH)_2[Al_{0.22}\ Si_{3.78}]_4\ O_{10}H_2O$ |
| (nascent stage) | 162 | $(Na_{0.12}\ K_{0.28}\ Ca_{0.07})_{0.47}(Mg_{0.34}\ Fe^{2+}_{0.64}\ Fe^{3+}_{0.03}\ Al_{1.11})_{2.12}\ (OH)_2[Al_{0.2}\ Si_{3.8}]_4\ O_{10}H_2O$ |
| Contact zone | 14 | $(Na_{0.01}\ K_{0.75}\ Ca_{0.03})_{0.8}(Mg_{0.41}\ Fe^{2+}_{0.7}\ Fe^{3+}_{0.94}\ Al_{0.09})_{2.14}\ (OH)_2\ [Al_{0.3}\ Si_{3.7}]_4\ O_{10}H_2O$ |
| (evolved stage) | 31 | $(Na_{0.03}\ K_{0.74}\ Ca_{0.03})_{0.8}(Mg_{0.41}\ Fe^{2+}_{0.71}\ Fe^{3+}_{0.94}\ Al_{0.1})_{2.16}\ (OH)_2\ [Al_{0.24}\ Si_{3.76}]_4\ O_{10}H_2O$ |

calculate $Fe^{3+}$ and $Fe^{2+}$ contents for silicates and Ti-Fe oxide minerals analyzed using EPMA. The calculated formulas (Table 3) show that the compositional range of the octahedral sheet in the Hanabad Fm green clay glauconite and the octahedral sheet of the contact zone glauconite were characterized by a high number of Fe atoms. There were 0.66 Fe atoms per formula unit (a.p.f.u) in the green clay (0.63 $Fe^{2+}$ and 0.03 $Fe^{3+}$) and 1.66 Fe atoms in the glauconite from the contact zone (0.7 $Fe^{2+}$ and 0.94 $Fe^{3+}$). The number of octahedral sheet A1 in the mineral formulas decreased from 1.04 Al in the green clay to 0.1 Al in the contact zone glauconite. The number of Mg atoms ranged from 0.35 in the Hanabad Fm to 0.41 per $O_{10}(OH)_2$ in the contact zone, which corresponds to an ordered glauconite with 0.30 to 0.40 Mg (Odom, 1984). The number of tetrahedral Al atoms ranged from 0.20−0.22 in the green clay to 0.24−0.30 in the contact zone samples. The green clay contained more Si (3.78−3.80) than the contact zone glauconite (3.70−3.76).

In comparison to the 2.00 octahedral cations in an ideal formula unit, the octahedral cation sums were 0.13 and 0.14 units larger in the green clay (2.13) in the contact zone (2.14) glauconites, respectively. However, the sums of the alkali cations (K, Na, Ca) in the mineral formulas (*i.e.* total layer charge) were considerably lower than in the ideal formula (1.00) and were 0.5 in the green clay glauconite and 0.8 in the contact zone glauconite samples. This implied that some of the $Fe^{3+}$ was in free iron oxides and was not part of the glauconite structure (Grunner, 1935; Strickler and Ferrell, 1990). Thompson and Hower (1975) showed that glauconites with less than 5% expandable layers have ~0.75 K atoms per $Si_4O_{10}$ formula unit in the evolved stage, while glauconites with more expandable layers (>10%) have ~0.3 K atoms in the nascent stage (Figure 12). The calculations herein indicated that the average number of K atoms per formula unit increased from ~0.3 in the green clay to ~0.75 in the contact zone formation. In Figure 12 (Meunier and El Albani, 2007), the samples mainly contain smectite, MLM, and glauconite phases. The data on the contact zone glauconite indicate a mineral phase near the edge of the glauconite field in Figure 12 with high (K+Na+Ca)/Si and Fe/Sum of

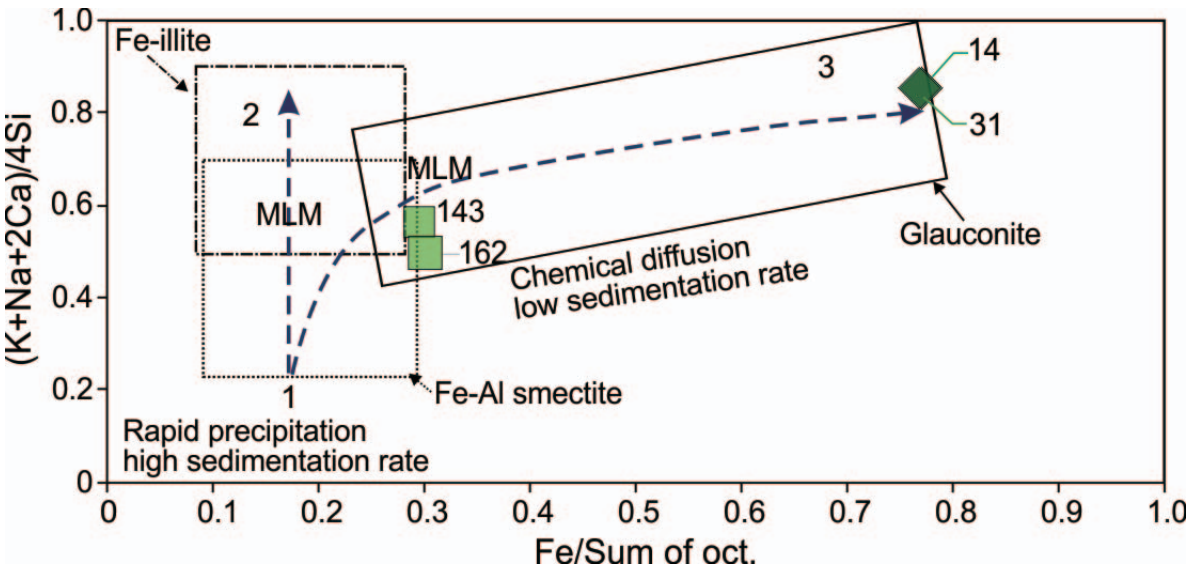


Figure 12. The compositional domains of Fe-bearing clay phases from samples plotted using the (K+Na+Ca)/Si *vs* Fe/Sum of octahedral cation coordinates used by Meunier and El Albani (2006). Mineral samples were plotted in the (1) Fe-Al smectite, (2) Fe-illite, and (3) glauconite zones. The (K+Na+Ca)/Si ratio corresponds to the interlayer charge (Na + K + 2Ca) divided by Si/4. MLM = mixed-layered mineral. Samples 31 and 14 were from the contact zone, samples 143 and 162 were from the Hanabad Fm, and samples 244 and 199 were from the yellow clay.

Table 4. Glauconitic-sample EMPA data for samples from the Paleogene Hanabad Fm green clay and the contact zone.

| | Samples from the contact zone | | | | | | | | | | | | | | | | | |
|---|---|---|---|---|---|---|---|---|---|---|---|---|---|---|---|---|---|---|
| | 14 | 31 | | | | | | | | | | | | | | | | |
| $SiO_2$ | 49.54 | 49.29 | 49.33 | 51.52 | 48.62 | 49.50 | 49.72 | 48.39 | 48.98 | 49.41 | 49.00 | 48.98 | 49.11 | 49.30 | 49.26 | 49.25 | 48.81 | 49.22 |
| $TiO_2$ | 0.19 | 0.06 | 0.06 | 0.00 | 0.03 | 0.02 | 0.09 | 0.00 | 0.00 | 0.09 | 0.01 | 0.07 | 0.04 | 0.01 | 0.00 | 0.02 | 0.00 | 0.03 |
| $Al_2O_3$ | 4.40 | 3.81 | 4.36 | 3.75 | 4.08 | 4.38 | 4.77 | 3.57 | 3.74 | 4.95 | 5.07 | 2.81 | 4.72 | 4.05 | 3.78 | 3.72 | 3.69 | 4.32 |
| FeO | 27.00 | 26.63 | 26.66 | 26.48 | 26.78 | 25.81 | 25.70 | 26.20 | 26.47 | 24.79 | 25.38 | 28.45 | 24.86 | 25.93 | 27.20 | 26.77 | 27.11 | 25.59 |
| MnO | 0.08 | 0.06 | 0.06 | 0.08 | 0.13 | 0.06 | 0.07 | 0.10 | 0.16 | 0.13 | 0.06 | 0.04 | 0.11 | 0.15 | 0.13 | 0.11 | 0.10 | 0.11 |
| MgO | 3.71 | 3.57 | 3.66 | 3.39 | 3.50 | 3.74 | 3.75 | 3.76 | 3.82 | 3.81 | 3.63 | 3.52 | 3.86 | 3.84 | 3.95 | 3.94 | 3.74 | 3.95 |
| CaO | 0.34 | 0.32 | 0.33 | 0.26 | 0.35 | 0.28 | 0.30 | 0.24 | 0.22 | 0.23 | 0.27 | 0.20 | 0.27 | 0.26 | 0.20 | 0.23 | 0.26 | 0.31 |
| $Na_2O$ | 0.09 | 0.20 | 0.03 | 0.04 | 0.06 | 0.04 | 0.06 | 0.02 | 0.02 | 0.04 | 0.03 | 0.19 | 0.01 | 0.00 | 0.07 | 0.04 | 0.05 | 0.01 |
| $K_2O$ | 7.82 | 7.56 | 8.02 | 7.85 | 7.98 | 7.99 | 8.11 | 8.20 | 8.35 | 8.39 | 8.56 | 8.03 | 8.43 | 8.53 | 8.35 | 8.35 | 8.37 | 8.43 |
| $Cr_2O_3$ | 0.01 | 0.01 | 0.00 | 0.02 | 0.00 | 0.00 | 0.00 | 0.00 | 0.00 | 0.01 | 0.00 | 0.00 | 0.00 | 0.00 | 0.01 | 0.00 | 0.05 | 0.03 |

| | Samples from the contact zone | | | | | | | | | | | | Green clay from the Hanabad Fm | | | | |
|---|---|---|---|---|---|---|---|---|---|---|---|---|---|---|---|---|---|
| | 1511 | | | | | | | | | | | | 257 | 1542 | $1542_1$ | 143 | **162** |
| $SiO_2$ | 50.56 | 50.87 | 48.13 | 50.43 | 49.05 | 49.41 | 50.69 | 52.06 | 50.44 | 49.01 | 51.12 | 49.57 | 49.02 | 48.37 | 53.58 | 44.70 | 54.17 | 56.66 |
| $TiO_2$ | 0.04 | 0.06 | 0.04 | 0.11 | 0.00 | 0.03 | 0.02 | 0.10 | 0.07 | 1.66 | 0.00 | 0.02 | 0.03 | 0.96 | 0.34 | 0.42 | 0.76 | 0.78 |
| $Al_2O_3$ | 4.55 | 5.15 | 2.48 | 5.18 | 2.82 | 3.26 | 4.53 | 6.39 | 4.57 | 4.03 | 5.90 | 3.97 | 3.89 | 21.99 | 22.52 | 17.38 | 14.64 | 16.64 |
| FeO | 25.70 | 26.01 | 29.17 | 25.97 | 28.89 | 28.03 | 27.02 | 23.59 | 27.37 | 26.39 | 25.60 | 27.56 | 27.50 | 6.26 | 6.10 | 5.96 | 6.65 | 7.03 |
| MnO | 0.04 | 0.09 | 0.06 | 0.07 | 0.12 | 0.01 | 0.08 | 0.02 | 0.06 | 0.05 | 0.05 | 0.17 | 0.11 | 0.01 | 0.04 | 0.02 | 0.04 | 0.04 |
| MgO | 3.71 | 3.75 | 3.50 | 3.89 | 3.48 | 3.66 | 3.73 | 3.00 | 3.67 | 3.57 | 3.75 | 3.77 | 3.69 | 3.79 | 3.73 | 3.66 | 3.53 | 3.41 |
| CaO | 0.38 | 0.27 | 0.13 | 0.35 | 0.13 | 0.24 | 0.35 | 0.32 | 0.28 | 0.39 | 0.41 | 0.24 | 0.25 | 0.56 | 0.68 | 0.73 | 1.58 | 0.96 |
| $Na_2O$ | 0.29 | 0.07 | 0.28 | 0.04 | 0.25 | 0.06 | 0.09 | 0.27 | 0.09 | 0.13 | 0.09 | 0.10 | 0.10 | 0.26 | 0.10 | 0.67 | 0.81 | 0.94 |
| $K_2O$ | 6.91 | 7.93 | 7.92 | 8.00 | 7.89 | 7.86 | 7.82 | 9.04 | 7.80 | 7.66 | 7.56 | 8.08 | 7.88 | 3.64 | 3.78 | 3.46 | 3.19 | 3.24 |
| $Cr_2O_3$ | 0.01 | 0.00 | 0.04 | 0.02 | 0.02 | 0.01 | 0.01 | 0.00 | 0.02 | 0.00 | 0.06 | 0.06 | 0.02 | 0.06 | 0.06 | 0.04 | 0.07 | 0.14 |

octahedral cation coordinate values. This illustrates complete glauconitization. The Hanabad Fm green clay samples fell into the glauconite-smectite MLM phase. This shows the beginning stages of glauconitization that were possibly interrupted by other processes. Additionally, Meunier and El Albani (2007) mentioned that the Fe–Al smectite composition domain is on the border between a Fe/Sum of octahedral cation ratio between 0.12 and 0.25 and for a $(Na^{+}+K^{+})/4Si$ ratio between 0.3 and 0.7. The sample Fe/Sum octahedral cation ratios (0.56 and 0.50) were higher than what Meunier and El Albani (2007) deduced, and clearly denotes a glauconite-smectite MLM phase (Figure 12). Two different stages of glauconite evolution in the green clay and the contact zone clay suggest that glauconite has slowly formed from expandable layers to produce the mica-like structure of glauconite during the initial to final part of Hanafad Fm deposition until the start of Sumsar Fm deposition.

## DISCUSSION

### *Evolution of glauconite*

As Harding (2014) mentioned, glauconite evolution produces a continuum of minerals from a K-poor disordered (nascent stage) glauconite to a K-rich ordered glauconite (evolved stage). Glauconite evolution is divided into various stages that depend on K content, pellet morphology, and crystalline structure. In Figure 13, the glauconites from the Hanabad Fm (samples 143, 162, and T1542) plot in the nascent stage, while glauconite from the contact zone (samples 14 and 31) plot in the evolved to highly evolved stages (Kim and Lee, 2000). The expandable layers indicated by the broad basal reflection at 10.57 Å (air-dried) in the green clay glauconite–smectite MLM (~3.5% $K_2O$) was replaced by an intense 10.04–9.8 Å reflection (air-dried) in the highly evolved contact zone glauconite grains (7–8.5% $K_2O$) (Figures 6d, 6e). Along with isomorphic substitutions, layer charge gradually increases, and more of the expandable layers eventually collapse from 10.57 Å to 10.04–9.8 Å (air-dried) to a mica-like structure as more K is taken into the structure. The transformation from expandable clay to glauconite requires K from the dissolution of surrounding K-feldspars, such as the microcline detected in the Isfara and Hanabad Fms. Glauconite has high Fe and K contents and the structure consists mainly of non-expandable layers (10 Å) (Hower, 1961; Tapper and Fanning, 1968). The total $Fe_2O_3$ content in glauconite from the Hanabad Fm (green clay) was ~7%, which increased to about 29% in the contact zone sample. An Fe source for glauconite may have been from the oxidation of pyrite. As mentioned above, an evolved glauconite may contain a small amount of smectite in a MLM (Figures 6 and 11). All the samples display a compositional evolution from the nascent (green clay) stage of glauconite to the evolved stage (Figures 12 and 13) (Odin and Matter, 1981; Odin, 1988; Giresse and Wiewióra, 1999; Dooley, 2006; Meunier and El Albani, 2007; Chang *et al*., 2008). Thus, based on the microscopic, mineralogical, and chemical analyses in the present study, the stages of glauconite maturity in the Kyzyltokoy basin can be summarized as follows: 1) the nascent stage is in the Hanabad Fm green clay; and 2) the evolved to highly evolved stages are in the contact

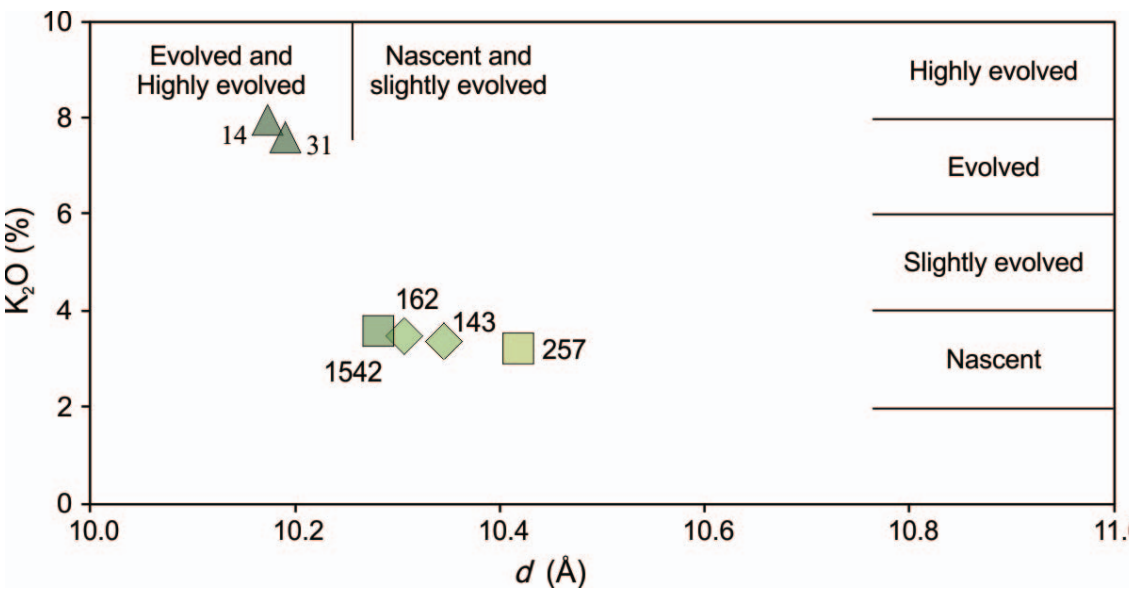


Figure 13. Correlation between the $d_{001}$ (Å) XRD peaks and the $K_2O$ contents (wt.%) of the glauconite samples from the Kyzyltokoy basin. Samples 253, 162, 143, and T1542 are from the Hanabad Fm green clay, whereas the 31 and 14 samples are from the contact zone between the Hanabad and the Sumsar Fms.

zone between the Hanabad and Sumsar Fms. The glauconite grains were finer, had a light-green color (Figure 3b), had less $K_2O$ (~3.5%), less Fe (~7%), and more expandable layers (~10.57 Å) during the nascent stage of the Hanabad Fm green clay (Figures 4, 6d, and 13). In the contact zone, glauconite grains with 6.5–9% $K_2O$ (Figure 9) and 29% total $Fe_2O_3$ had a micaceous structure with intense reflections at 10.04–9.98 Å (air-dried) and were in the evolved to highly evolved stages (Figures 6e and 13) (Odin, 1988; Kim and Lee, 2000; Holland and Turekian, 2004).

*Sedimentary environment of glauconitization*

Silicate formation is usually initiated by the recrystallization of an opaline silica material, which makes up the skeletons of Si-containing organisms and often occurs as a hydrated amorphous form of silica (Savko *et al*., 2001). In the Isfara Fm, the rocks were probably compacted and diatomites were formed as the silica crystallized. As the main component of diatomites, opal was not identified in XRD patterns, probably because opaline silica is X-ray amorphous or non-crystalline. That the deposition environment pH during Isfara Fm deposition was possibly high (8–9) is noteworthy, as evidenced by the presence of smectites and trace zeolites. The pH increase may have caused silica dissolution and redistribution in sediments and led to the formation of siliceous rocks and smectites. Sediment consolidation and smectite formation possibly resulted in the deeper parts of the Isfara Fm basin (several hundred m) due to the higher pressure (Compton, 1991; Savko *et al*., 2001). The interlayered diatomite-argillaceous rocks that appeared in the upper part of the Isfara Fm were dominated by smectite and a mica-like mineral (illite/or glauconite) and indicates that the rocks were altered from a diatomaceous to a clayey material.

The Rishtan and Isfara Fm samples had chemical compositions that indicated illite as a mica-like mineral, while the samples from the Hanabad Fm and contact zone were mainly glauconite (Figures 5 and 12). According to the Sumsar Fm depositional environment, glauconite was dissolved and the mica-like mineral should have been illite. The MLM series in the green clay and the contact zone were glauconite-smectites (Figures 8b and 11) (Velde, 1976). The higher MLM content of the Hanabad Fm green clay resulted from an interruption in the glauconitization process (Giresse and Wiewióra, 1999). Gupta and Malik (1969) proposed the chloritization of smectite by co-precipitation with Mg hydroxides. According to the Odin (1988) assumption that no substrate is similar to the mica-like structure and no substrate can recrystallize to form glauconite, present results lead to the conclusion that chlorite in the contact zone may have formed during smectite recrystallization into glauconite as an authigenic secondary mineral. The high gypsum contents in the samples were confirmed by XRD patterns of the yellow and green clays. Gypsum may have formed *in situ* by the reaction of sulfates with biogenic carbonates in the sediments (Czerewko and Cripps, 2006). Siesser and Rogers (1976) believed that such conditions may have prevailed along the continental slope during the late Miocene to early Pliocene regression, which provided a suitable environment for glauconitization.

The ferric and ferrous Fe contents of the glauconite grains from the contact zone (Tables 2, 3, 4) suggest that the environment was partially reducing and sub-oxic during glauconite formation. Harder (1980) pointed out that the "iron and aluminum of detrital minerals may dissolve in reducing microenvironments and precipitate during oxidizing process." Under reducing conditions, Fe is stable in the soluble ferrous state and can be fixed in authigenic silicates (smectites) as ferric Fe during oxic conditions over a pH range of neutral to alkaline. Reducing conditions may be imposed by bacterial activity, while oxidation can occur after bacterial activity ceases and organic matter is totally oxidized (Giresse and Wiewióra 2001; Giresse and Grabska, 2004; Gaudin *et al*., 2005). Under the reducing conditions imposed by bacterial activity, pyrite was likely precipitated and later dissolved during the oxidation process that led to Fe precipitation (Gaudin *et al*., 2005, Charpentier *et al*., 2011). Hence, organic matter may have played an important role in glauconite formation. The decreases in CaO content with increases in $K_2O$ (Figure 7f) suggest that carbonaceous nano-fossils may have been a substrate for glauconite formation (Odin, 1988; Amorosi *et al*., 2007). The light green margins and spots on the glauconite grains, which have low Fe and K contents but high Al contents, indicate that the grains likely disintegrated by chemical weathering. The phenomenon of glauconite lixiviation (*i.e*. leaching with a solvent) has been reported in the literature (Loveland, 1981; Skiba *et al*., 2014; Franzosi *et al*., 2014). A strongly oxidizing environment may have caused glauconite dissolution and the formation of Fe oxides or oxyhydroxides (such as hematite) during the formation of the Sumsar Fm (Berner, 1981; Kelly and Webb, 1999; Huggett *et al*., 2017).

In brief, three different deposition environments may have been involved in the Paleogene Fms of the Kyzyltokoy basin. In the Isfara and Hanabad Fms, the glauconitization process was interrupted before completion (Meniuer and Albani, 2007), which was implied by the nascent glauconite mineral identified in the formations. The glauconitization process was complete in the contact zone, *i.e*., between the top of the Hanabad and the bottom of the Sumsar Fms, but glauconite may have decomposed during the development of the Sumsar Fm.

## CONCLUSIONS

The present study demonstrated that glauconite in the Kyzyltokoy basin likely formed *via* a precipitation-

dissolution-recrystallization mechanism. Diatomite alteration to produce smectitic diatomite-argillaceous rocks suggests that the glauconite precursor was likely a siliceous mineral. While a decreased CaO content and an increased $K_2O$ content in the Hanabad Fm green clay may imply that carbonaceous nano-fossils could also be a plausible substrate. The substrate for glauconite formation, however, has remained an open question that merits further studies.

The formulas of glauconite minerals at different maturity stages were calculated from the chemical compositions. Two maturity stages (nascent and evolved) were revealed in the Paleogene Fms of the Kyzyltokoy basin. Glauconite maturity is determined from the $K^+$ and $Fe^{3+}$contents. Nacent stage glauconite has more expandable layers, but lower $K^+$ and $Fe^{3+}$ contents than an evolved glauconite.

Three different depositional environments, hence, were present during the formation of the Paleogene Fms in the Kyzyltokoy basin: 1) a glauconitization process that was interrupted before completion; 2) a favorable environment for complete glauconitization; and 3) glauconite decomposition.

## ACKNOWLEDGMENTS

The authors thank M. Usenov, A.T. Kenjebaev, and A. Tugenbaev for their field support, and G. Bekenova, A. Bakirov, and the staffs from the University of Shimane (Japan) and Arctic University (Norway) for the lab analyses. This manuscript was jointly supported by the key project of National Natural Science Foundation of China (41230316), the National 973 Program of China (2014CB440906), and the Scholarship for International Students of UCAS (University of Chinese Academy of Science).

## REFERENCES

Afanasjeva, N.I., Zorina, S.O., Gubaidullina, A.M., Naumkina, N.I., and Suchkova, G. (2012) Crystal chemistry and genesis of glauconite from "Melovatka" section (Cenomanian, of South-Eastern Russian plate). *Lithosphera*, **2**, 65–75.

Amorosi, A. (1997) Detecting compositional, spatial, and temporal attributes of glaucony: A tool for provenance research. *Sedimentary Geology*, **109**, 135–153.

Amorosi, A., Guidi, R., Mas, R., and Falanga, E. (2011) Glaucony from the Cretaceous of the Sierra de Guadarrama (central Spain) and its application in a sequence-stratigraphic context. *International Journal of Earth Sciences*, **101**, 415–427.

Amorosi, A., Sammartino, I., and Tateo, F. (2007) Evolution patterns of glaucony maturity: A mineralogical and geochemical approach. *Deep Sea Research Part II: Topical Studies in Oceanography*, *54*, 1364–1374.

Bakirov, A.B., Mezgin, I..A., Bektemirova, T.A., and Usenov, M. (2011) The structure of Paleogene within the Kyzyltokoy depression (Southern foot of Chatkal Rridge). *Izvestiya*, National Academy of Science of Kyrgyz Republic, **2**, 81–83.

Berner, R.A. (1981) A new geochemical classification of sedimentary environments. *Journal of Sedimentary Petrology*, **51**, 359–365.

Burst, J. (1958) Mineral heterogeneity in glauconite pellets. *American Mineralogist*, **43**, 481–497.

Chang, S.S., Shau, Y.H., Wang, M.K., Ku, T.K., and Chiang, P.N. (2008) Mineralogy and occurrence of glauconite in central Taiwan. *Applied Clay Science*, **42**, 74–80.

Charpentier, D., Buatier, M. D., Jacquot, E., Gaudin, A., and Wheat, C. G. (2011) Conditions and mechanism for the formation of iron-rich montmorillonite in deep sea sediments (Costa Rica margin): Coupling high resolution mineralogical characterization and geochemical modeling: *Geochimica et Cosmochimica Acta*, **75**, 1397–1410.

Compton, J.S. (1991) Origin and diagenesis of clay minerals in the Monterey formation, Santa Maria Basin area, California. *Clays and Clay Minerals*, **39**, 449–466.

Czerewko, M. A. and Cripps, J. C. (2006) Sulfate and sulfide minerals in the UK and their implications for the built environment. *The Geological Society of London*, IAEG2006 paper number 121.

Dooley, J.H. (2006) Glauconite. Pp. 495–506 in: *Industrial Minerals & Rocks: Commodities, Markets, and Uses* (J. Kogel, N. Trivedi, J. Barker, and N. Krukowski, editors). Society for Mining, Metallurgy, and Exploration, Littleton, Colorado, USA.

Franzosi, C., Castro, L.N., and Celeda, A.M. (2014) Technical evaluation of glauconies as alternative potassium fertilizer from the Salamanca Formation, Patagonia, Southwest Argentina. *Natural Resources Research*, **23**, 311–320.

Gaudin, A., Buatier M.D., Beaufort, D., Petit S., Grauby, O., and Decarreau, A. (2005) Characterization and origin of $Fe^{3+}$-montmorillonite in deep water calcareous sediments (Pacific Ocean, Costa Rica margin). *Clays and Clay Minerals*, **53**, 452–465.

Giresse, P. and Wiewióra, A. (1999) Origin and diagenesis of blue-green clays and volcanic glass in the Pleistocene of the Côte d'Ivoire Ghana marginal ridge (odp leg 159, site 959). *Sedimentary Geology*, **127**, 247–269.

Giresse, P. and Wiewióra, A. (2001) Stratigraphic condensed deposition and diagenetic evolution of green clay minerals in deep water sediments on the Ivory Coast–Ghana Ridge. *Marine Geology*, **179**, 51–70.

Gruner, J.W. (1935) The structural relationship of glauconite and mica. *American Mineralogist*, **20**, 699–714

Gupta, G.C. and Malik, W.U. (1969) Chloritization of montmorillonite by its coprecipitation with magnesium hydroxide. *Clays and Clay Minerals*, **17**, 331–338.

Harder, H. (1980) Synthesis of glauconite at surface temperatures. *Clays and Clay Minerals*, **28**, 217–222.

Harding, S.C., Nash, B.P., Petersen, E.U., Ekdale, A.A., Bradbury, C.D., and Dyar, M.D. (2014) Mineralogy and geochemistry of the main glauconite bed in the middle Eocene of Texas: Paleoenvironmental implications for the verdine facies. *PloS One*, **9**, e87656.

Hower, J. (1961) Some factors concerning the nature and origin of glauconite. *American Mineralogist*, **46**, 313–334.

Huggett, J., Adetunji, J., Longstaffe, F., and Wray, D. (2017) Mineralogical and geochemical characterization of warm-water, shallow-marine glaucony from the Tertiary of the London basin. *Clay Minerals*, **52**, 25–50.

Keller, W. (1958) Glauconitic mica in the Morrison Formation in Colorado. *Clays and Clay Minerals*, **5**, 120–128.

Kelley, W.P. (1952) Interpretation of Chemical Analyses of Clays. *Clays and Clay Minerals*, **1**, 92–94.

Kelly, J.C. and Webb, J.A. (1999) The genesis of glaucony in the Oligo–Miocene Torquay Group, southeastern Australia: Petrographic and geochemical evidence. S*edimentary Geology*, **125**, 99–114.

Kim, Y. and Lee, Y.I. (2000) Ironstones and green marine clays in the Dongjeom Formation (Early Ordovician) of Korea. *Sedimentary Geology*, **130**, 65–80.

Longuépée, H. and Cousineau, P.A. (2006) Constraints on the

genesis of ferrian illite and aluminum-rich glauconite: Potential impact on sedimentology and isotopic studies. *The Canadian Mineralogist*, **44**, 967–980.

Loveland, P.J. (1981) Weathering of a soil glauconite in southern England. *Geoderma*, **25**, 35–54.

Meunier, A. and El Albani, A. (2007) The glauconite-Fe-illite-Fe-smectite problem: A critical review. *Terra Nova*, **19**, 95–104.

Moore, D.M. and Reynolds, R.C. (1997) Identification of clay minerals and associated minerals. Chapter 6, pp. 202–240 in: *X-ray Diffraction and the Identification and Analysis of Clay Minerals*, Oxford University Press, New York.

Odin, G.S. (1990) Clay mineral formation at the continent-ocean boundary: The verdine facies. *Clay Minerals*, **25**, 477–483.

Odin, G.S. (1988) (editor) Green Marine Clays: Oolitic Ironstone Facies, Verdine Facies, Glaucony Facies and Celadonite-Bearing Rock Facies – A Comparative Study. *Developments in Sedimentology*, **45**, Elsevier, Amsterdam.

Odin, G.S. and Fullagar, P.D. (1988) Green Marine Clays: Chapter C4 Geological significance of the glaucony facies. *Developments in Sedimentology*, **45**, Elsevier, Amsterdam, 295–332.

Odin, G.S. and Matter, A. (1981) Origin of glauconites. *Sedimentology*, **28**, 611–641.

Odom, I.E. (1984) Glauconite and celadonite minerals. *Biochemical Journal*, **319**, 117–122.

Savko, A., Zhabin, A., and Dmitriev, D. (2001) The morphology of zeolite particles of the heulandite group and minerals free of silica in sediments of the Voronezh anteclise: Vestnik, Voronezh State University. *Geology*, **12**, 51–56.

Siesser, W.G. and Rogers, J. (1976) Authigenic pyrite and gypsum in South West African continental slope sediments. *Sedimentology*, **23**, 567–577.

Skiba, M., Maj-Szeliga, K., Szymański, W., and Błachowski, A. (2014) Weathering of glauconite in soils of temperate climate as exemplified by a Luvisol profile from Góra Puławska, Poland. *Geoderma*, **235–236**, 212–226.

Strickler, M.E. and Ferrell, R.E., Jr. (1990) Fe substitution for Al in glauconite with increasing diagenesis in the first Wilcox sandstone (lower Eocene), Livingston Parish, Louisiana. *Clays and Clay Minerals*, **38**, 69–76.

Tapper, M. and Fanning, D. (1968) Glauconite pellets: Similar X-ray patterns from individual pellets of lobate and vermiform morphology. *Clays and Clay Minerals*, **16**, 275–283.

Thompson, G.R. and Hower, J. (1975) Mineralogy of glauconite. *Clays and Clay Minerals*, **23**, 289–300.

Velde, B. (1976) The chemical evolution of glauconite pellets as seen by microprobe determinations. *Mineralogical Magazine*, **40**, 753–760.

Velde, B. and Odin, G. (1975) Further information related to the origin of glauconite. *Clays and Clay Minerals*, **23**, 376–381.

Vyalov, O.S. (1947) A comparison of the Paleogene formations of Turkmenistan with the Caucasus and Central Asian Paleogene formations. *Izvestiya*, National Academy of Science of the USSR, **3**, 158.

Wiewióra, A., Giresse, P., Petit, S., and Wilamowski, A. (2001) A deep-water glauconitization process on the Ivory Coast–Ghana marginal ridge (ODP site 959): Determination of $Fe^{3+}$-rich montmorillonite in green grains. *Clays and Clay Minerals*, **49**, 540–558.

Zheng, Q. (1983) Calculation of the $Fe^{2+}$ and $Fe^{3+}$ contents in silicate and Ti-Fe oxide minerals from EPMA data. *Acta Mineralofica Sinica*, **3:**55–62.

(*Received 3 July 2017; revised 12 February 2018; Ms. 1187; AE: J. Zhu*)